Unweaving dendrite formation through in operando synchrotron X-ray diffraction study of individual lithium crystallites

R.E.D. van de Lagemaat

Report of master thesis project carried out at
Group: Storage of Electrochemical Energy
Department: Radiation Science & Technology

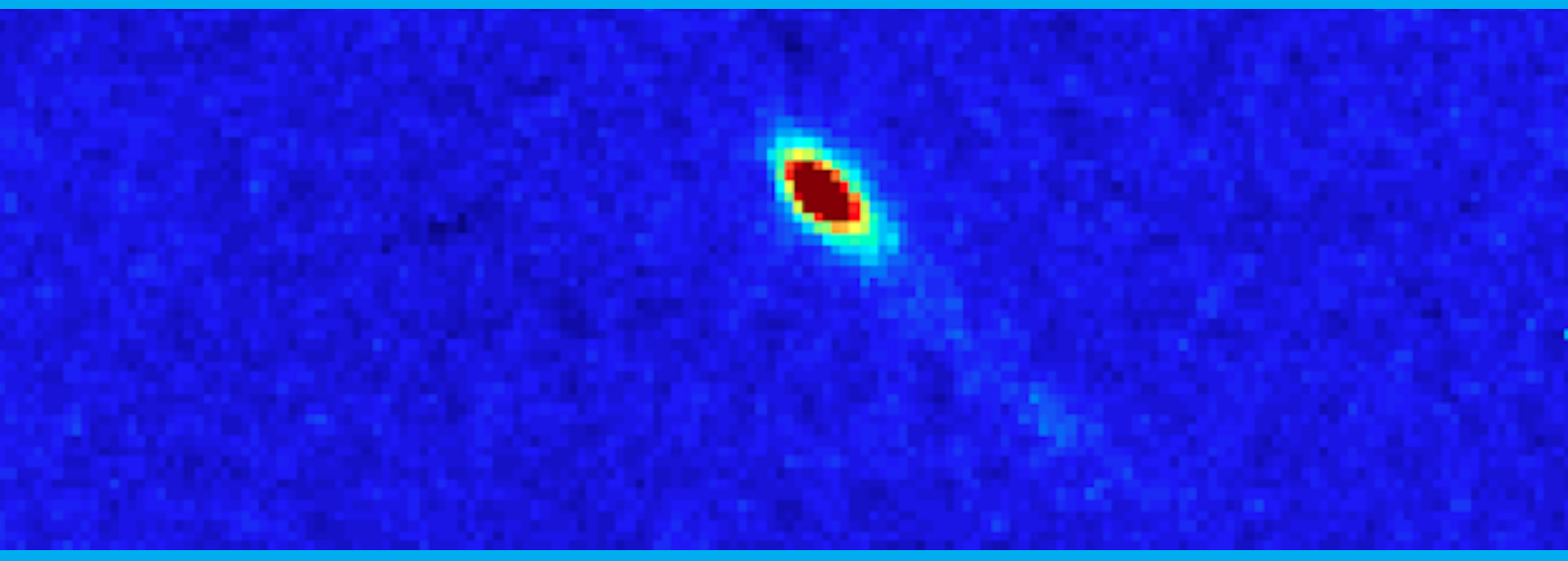

Unweaving dendrite formation through in operando synchrotron X-ray diffraction study of individual lithium crystallites

by

R.E.D. van de Lagemaat

to obtain the degree of Master of Science in Sustainable Energy Technology
at the faculty of Electrical Engineering, Mathematics and Computer Science (EEMCS),
Delft University of Technology,
to be defended publicly on Thursday March 15, 2018 at 10:00 AM.

Student number:	4496442	
Project duration:	July 1, 2017 – March 15, 2018	
Thesis committee:	Dr. ir. M. Wagemaker,	TU Delft, supervisor
	Prof. Dr. C. Papas,	TU Delft
	Dr. Ir. A. van Well,	TU Delft

This thesis is confidential and cannot be made public until March 15, 2018.

TU Delft

Unweaving dendrite formation through in operando synchrotron X-ray diffraction study of individual lithium crystallites

R.E.D. van de Lagemaat†

† *Department of Radiation Science and Technology, Delft University of Technology, Mekelweg 15, 2629JB Delft, The Netherlands*

Abstract

In the search for renewable energy storage materials, lithium metal has been considered the ideal electrode material for decades, due to its high specific capacity. However, dendrite formation leading to poor cycling behaviour has seemed an insurmountable problem ever since. In recent years, advancements in observational- and nanotechnologies have allowed for the identification of many of the factors that influence dendrite formation, as well as many suggestions to overcome them. Obtaining further understanding of the fundamental processes at play in dendrite formation is crucial in developing the next generation lithium batteries. In order to investigate dendrite formation at the nanoscale, in operando synchrotron X-ray diffraction experiments were conducted. A pouch cell with a Li-Li symmetric cell using a $LiPF_6$ 1:1 EC:DMC electrolyte was used to perform the experiments. The growth rate of individual crystallites was determined, as well as the consumption of lithium crystallites by the electrolyte to form solid-electrolyte interphase (SEI). By determining the volume of individual crystallites over time, their formation and decay rate could be determined. Three categories were put forward to classify the types of behavior of individual crystallites during plating and relaxation. It was found that a significant part of dendrites show behaviour that is independent of the macroscopic current density.

Keywords: In Operando — Lithium Metal Anode — Synchrotron XRD — High Capacity Batteries — Dendrite

Introduction

The Paris agreement of 2015 marks a global recognition of the urgent need to curb greenhouse gas emissions. There are still many unresolved questions regarding our atmosphere and biosphere, but it seems almost certain that human-induced climate change will have long-lasting impacts on the planet [1,2]. It is therefore one of the main challenges of mankind to facilitate our energy needs from the 21st onward using renewable sources [3]. Storing energy chemically on long timescales is effective, as is evinced by our heavy reliance on fossil fuels. The transition from fossil fuel combustion to intermittent power production by sources such as wind and solar requires grid stabilization and supply-demand matching [4]. Storage of electrochemical energy can provide a non-polluting means of on-demand electrical energy at efficiencies exceeding that of combustion engines. Therefore, as our population expands and transportation is increasingly electrified, the demand for high energy density batteries continues to increase [5]. The research by Goodenough, Yazami and Yoshino among others culminated in the commercialization of the 'rocking chair' li-ion battery by Sony in 1991 [6,7]. This was a safe battery with a reasonably energy density and cycle life. A gravimetric energy density of up to 250 Wh kg^{-1} is possible despite a specific capacity of a mere 372 mAh g^{-1} of the graphite negative electrode, due to the high potential of over 3.6 V. This Li-ion chemistry would become the battery of choice for most commercial portable electronics, and more recently for electric vehicles [8,9]. Despite its large market share and significant R&D, the energy density of commercial Li-ion batteries has been only moderately increasing [10]. Therefore, other chemistries with higher theoretical energy density such as Si, Ge, Sn and Li negative electrodes and S and O_2 positive electrodes have been studied extensively [11]. Of these options lithium metal is the ultimate negative electrode, due to its high specific capacity of 3860 mAh g^{-1} and unrivaled potential of -3.04 V against the standard hydrogen electrode [12,13]. Being developed as primary batteries almost half a century ago, there seemed to be a bright future for lithium metal batteries (LMBs). However, the highly electropositive character of lithium comes at a cost. Lithium has a Fermi level that exceeds the lowest unoccupied molecular orbit (LUMO) of most organic electrolytes, causing the electrolyte to be reduced through which a solid-electrolyte inter-

phase (SEI) forms. This consumes substantial amounts of active material and leads to a reduced Coulombic efficiency (CE), a higher internal resistance and irreversible capacity loss[5]. Therefore, the forming of a stable SEI is crucial for the operation of Li based-batteries. Furthermore, lithium deposition on existing lithium is thermodynamically favorable over nucleation at the electrode, due to its low surface energy and low diffusion[10]. This causes a one-dimensional dendritic growth pattern which is the main challenge of producing highly cyclable LMB's. Both the dendritic growth and the low CE have already been identified as the main problems for LMBs since their inception[9,14]. The low CE can be accounted for by adding excess lithium[12]. However, repeated dendrite growth upon cycling can lead to dendrites penetrating the separator, making contact with the positive electrode and causing internal short-circuit. This leads to thermal runaway and fire and explosion hazards, which makes inhibition of dendrite growth of utmost importance on the path to commercialization[7].

Efforts to overcome the challenges of LMBs have increased as nano-technologies have opened up new ways to suppress dendrite growth and improve Coulombic efficiency, allowing LiM to be seen as a realistic contender for the next generation of batteries[12,15]. Four main strategies have been employed to inhibit dendrite formation[10]:

1. Alloying Li with eg. Al, Si or C to decrease the volume change upon cycling[16]
2. Organic electrolyte, optimizing SEI formation to passivate the Li[17]
3. Solid-state electrolytes, mostly inorganic ceramics or solid polymers[18]
4. Nanostructuring the LiM electrode to homogenize deposition[19]

Most attention has gone to tuning of the electrolyte, where different salts are to form an SEI with desired characteristics[20]. In the ideal circumstance, the SEI forms a thin layer that restricts Li plating to a flat surface, while ion conductivity is high and electric conductivity is low. However, due to the 'infinite' volume change when LiM is continuously cycled (due to the lack of a host matrix) , the SEI tends to crack. These cracks cause further reduction of the electrolyte and more inactive or 'dead' material leading to a decreased CE. Understanding the factors that play a role in dendrite formation and how to suppress them thus is critical in developing LMBs. The behavior of the Li electrode is well studied and simulated[21,22] and dendrite formation has been probed using a range of technologies, including SEM, NMR, AFM and X-ray tomography[18,22–25]. In-situ and operando studies of i-ion batteries have been conducted for well over a decade[26], and studies on LiM using operando XRD, video microscopy, and TXM have shed light on the formation of dendrites under several conditions[10,13,27–29]. However, this is the first time that LiM plating has been observed in operando at the level of individual crystals, through synchrotron X-ray diffraction on an LiM symmetric cell.

Experimental section

Cell fabrication: Symmetric pouch cells were fabricated for the experiment. The cell consists of a thin plasticized aluminum, within which there are consecutive layers of a copper current collector with a thickness of 18 μm, a lithium metal electrode of approximately 1 mm thickness with a diameter of 12.8 mm and a 1 mm hole punched in the center where the beam is pointed through, a 1M EC-DMC electrolyte, containing a 250 μm glassfibre micro-porous separator sandwiched in between two polyethylene slabs of 25 μm, and another 18 μm copper current collector. A hole was punched in the lithium metal as well as the outer part of the pouch, which was covered by a Kapton 'window', which has a high x-ray transmittivity.
Diffraction setup: At the ESRF beamline ID11 in Grenoble, the cells were placed in a lorentzian $\sim 5\mu m^2$ unpolarized monochromatic 45 KeV x-ray beam, as pictured schematically below. The small beam size was used to probe individual lithium grains forming over time. The high flux allowed for a short exposure time of 1 second to yield reflections with a sufficient signal/noise ratio. In order to prevent local electrolyte degradation, probing was done at four different spots, each point 100 micron away from the previous point. The sample was rotated along the z-axis over a 5 degree angle with frames taken every 0.5 degree steps. This allowed for a temporal resolution of approximately 110 seconds.
Data analysis: Each frame was stored as an ESRF data file (EDF) containing the observed intensity for each of the 2048x2048 pixels. This was analyzed in matlab to identify reflections over time. The volume and corresponding data was determined using a combination of known crystal properties such as the structure factor, in combination with DFT simulations to obtain the mean displacement at room temperature.

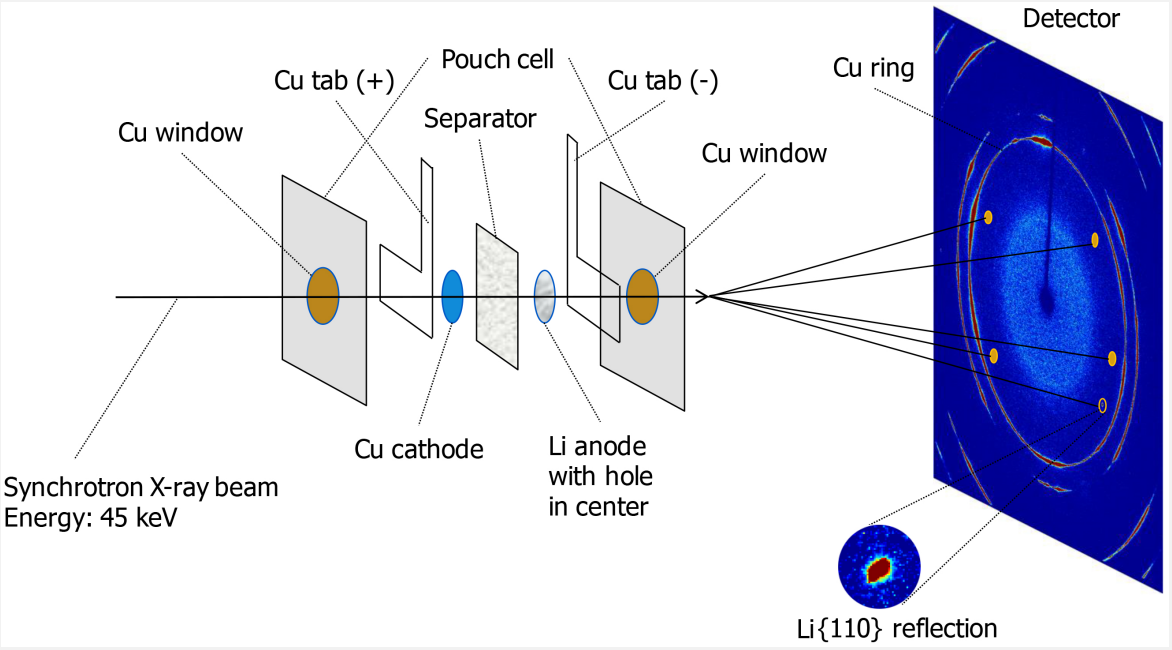

Results and discussion

The synchrotron beam allowed for a the in-operando observation of several individual crystals of a symmetrical Li-Li cell. The Li110 reflection is theoretically the strongest, which is supported by the fact that these reflections are observed at all points. The second highest intensity reflection Li211 is not observed. The symmetrical cell does not allow for meaningful voltage measurements to monitor the state of charge, therefore the main indicator of the 'state' of the battery is the applied current density. The current was set to 1 mA ($\sim$ 0.65 mA cm^{-2}), followed by a relaxation, both for a period of approximately one hour.

Nucleation

The rate of nucleation is given by Sand's time, and is dependent on the ionic mobilities, salt concentrations and current density. A higher current density predicts faster dendrite growth [22]. Grains were found within the first minute of the experiment, and this observation is not expected given the properties of lithium and the experimental setup.A current is required for Li-ions to migrate in a symmetrical cell, which was activated after the initial frames for each point and rotation angle were recorded. The diffusion of Li-ions through the electrolyte further retards the formation of dendrites. How and why these category A grains do appear instantly is not resolved. One reason could be that what is actually observed is lithium grains at the lithium anode side. However this was not conclusively shown as the standard deviation of the twotheta angles of grains within a category was larger than the difference between the means of each category.

Dendrite categories

The behavior of lithiation is known to be controlled by the composition of the SEI, the electrolyte, local electric fields and the interface with the current collector [10,12,18]. Despite the fact that these parameters all have similar values for different dendrites in a single battery with a low current density, a large variation was found in the development of individual crystallites. Based on these deviations, three groups are distinguished. The first group (A) consists of crystallites that show continuous decay throughout the plating cycle. Crystallites in group B are forming but stabilize and decay slightly before the plating cycle ends. Crystallites in group C are forming and growing continuously during the experiment. It is immediately evident that group A and group C are almost of opposite behavior.

It is remarkable to see that all identified grains fit so well into pre-determined groups. This indicates that there are different local states that dictate dendrite dynamics. Throughout the experiment the volume of category A dendrites continues to go down at a stable pace, as can be seen in the averaged plot of category a in figure 2a. Thus there seems to be no formation of a passivating SEI layer on these crystals, which may indicate a local instability of what is usually a stable layered structure, leading to continuous exposure of lithium to electrolyte compounds. Another factor at play may be the shape of the dendrite. The several dendrite structures as identified by [24], each have a surface to specific surface-volume ratio. It may be that grains in this category are of a particularly high ratio and are therefore more prone to electrolyte consumption. The observed grains in category B are following a growth pattern that is most in agreement with what theory would predict, as can be seen in figure 2b. However the length of over 30 micron is a factor 3 to 5 larger than the needle-like dendrites that were observed in previous studies using the same electrolyte chemistry [30]. Because the lithium is plated on copper rather than lithium as it would upon charging an LMB, so growth will be naturally from the tip. Grains of category B may be forming near contaminants in the SEI, as they show high initial growth rates and contaminants have been found to catalyze the growth of dendrites [30]. The growth pattern followed by stabilization and decay perhaps indicates that there is a critical size for dendrites in this electrolyte, and upon reaching it some instability in the SEI may cause the dendrite to be exposed to the electrolyte, leading to oxidation of the dendrite. Dendrites that are classified as category C show a continuous trend of increase over time, as can be seen in 2c. Growth of these dendrites is likely to be sustained by continuous passivation of SEI that is formed by lithium that is not in electronic contact with the observed grains. This may be due to a relatively thick layer of SEI forming in the vicinity, or due to a growth angle that is more in-plane with the SEI-lithium interface than other dendrites.

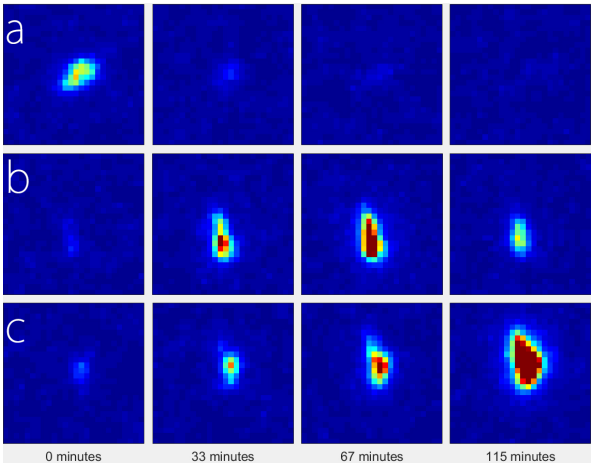

Figure 1: Development of a single grain over time that is representative of each category. **(*a*)** Dendrite in category A showing highest intensity at the start of the experiment, with a decay to near invisiblity after approximately half an hour, **(*b*)** a category B dendrite and **(*c*)** a category C dendrite forming continuously even during relaxation.

Growth Rate

The volume of individual grains was calculated as is explained in Appendix A, and the length of dendrites was determined assuming that it consists of a single crystal and using an average cross-section of $5 \cdot 10^4 nm^2$, based on an average of the surfaces as described by Li et al [24]. The three plots for the respective groups are shown in figure 2. The average growth rate of grains in C was determined to be 86 nm

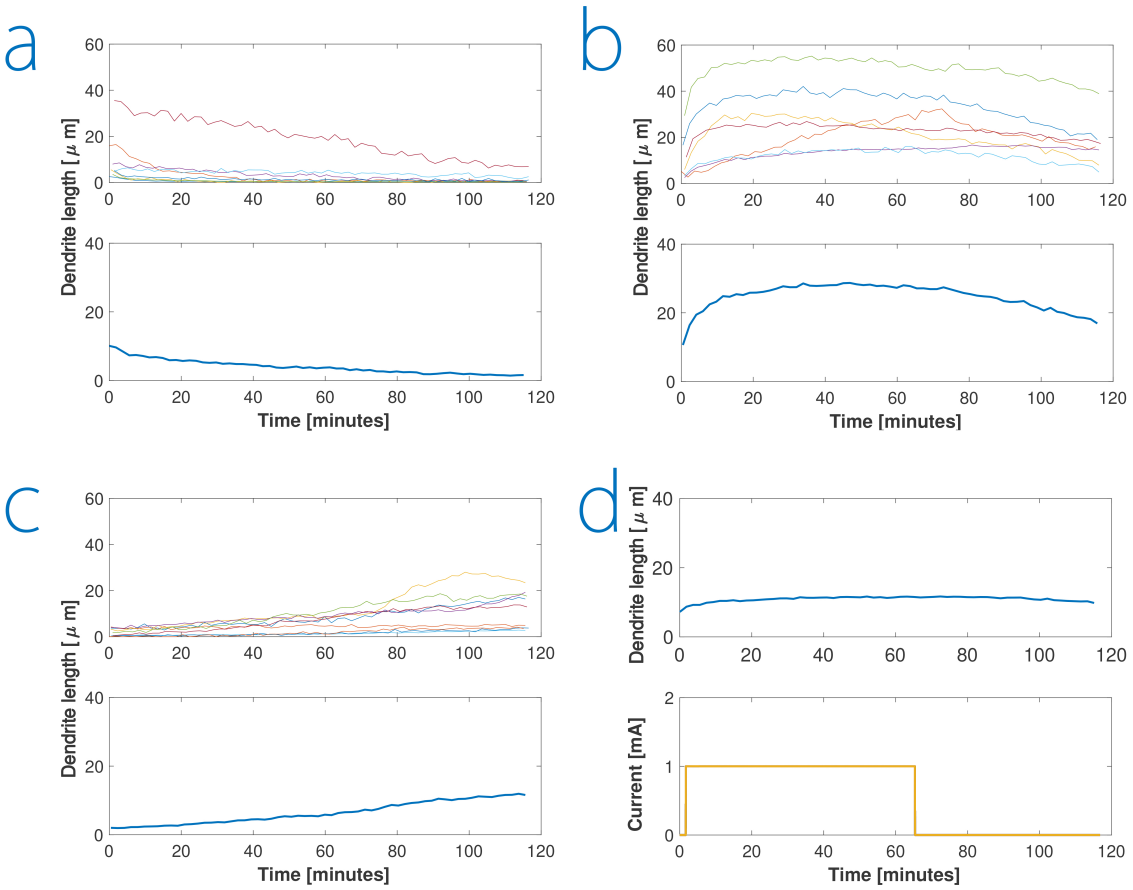

Figure 2: Three categories of grains showing from groups A, B C and an overall average. The top graph are individual crystals and the bottom graph shows the average of the category. (***a***) The dendrites in category A show one clear strongest reflection, being twice the size of the second largest dendrite in the category at its initial observation. All other grains follow the same pattern of constant decay. (***b***) The development of reflections in B shows a fast initial growth pattern, followed by a relatively stable period which slowly turns into decay. (***c***) Dendrites in C show a steady initial growth, which in all cases but one is followed by a continuation of growth at approximately that rate throughout the experiment. The exception (yellow line) shows a pattern that is a bit similar to that of category B grains, but with a late onset after a long constant slow-growth. (***d***) shows the average of all grains in the experiment. The general trend is that of category B, as this is a sort of average of A and C while B is also the strongest reflection. The lower graph shows the current of the experiment as a function of time, indicating plating for a little over an hour and relaxation for slightly less than an hour.

per minute. This is slightly lower than what has been found by earlier studies using NDP to determine the Li-density, where the growth rate was determined to be between 100-250 nm per minute[31]. This might be due to the less localized plating that is a consequence of the low current density. However, the average growth rate of dendrites in group B initially is very high at approximately 1 μm per minute, but then stabilizes and eventually even decays, which indicates that there may be another factor at play. The average decay rate of group A was found to be 69 nm per minute.

At the peak growth rate, and assuming growth perpendicular to the electrode surface, a dendrite could reach the other electrode in a mere five minutes even at this low current density. However, due to reactivity with the electrolyte, branching, fracture and the occurrence of kinks, this will not happen. The growth pattern of category B attests to this.

Stability

The timelapse image in figure 1 of individual grains from each category reveal the main trends of dendrites during the experiment. A more thorough analysis of the data can provide insight into the stability of the SEI within which the dendrites are located. Despite the obvious movement of Li-ions that form the basis of the fluctuations in dendrite

size over time, there is no indication of stresses causing dendrites to break or displace significantly. In both category A and B the observed decrease in integrated intensity may be both due to physical change in size and a displacement out of diffraction position of the respective dendrites. However if the latter were the case it is more likely to be an event that happens to specific grains and changes the reflection substantially in a short timeframe, whereas the observed intensities all show gradual changes over time. Furthermore there is no sign of Li_2CO_3 or Li_2O formation, indicating that these compounds do not form substantial crystalline structures in this electrolyte. This reveals that there is a high stability of the structure, which is in accordance with observations done in earlier studies [32].

Conclusion

In operando synchrotron diffraction was shown to be an effective way to probe lithiation. The Li110 reflection is theoretically the strongest, which is supported by the fact that these reflections are observed at all points. This is however the only Li reflection and therefore the results are limited to determining the volume, and not of preferred orientation of dendrites.

It was found that there are three categories of dendrite development, and it was hypothesized that their development over time is dictated by local fluctuations in SEI strength thickness, contaminant concentration and current density.

The overall trend of dendrite growth is a rapid initial growth followed by a saturation and a decay during relaxation. However, a substantial part of observed grains do not decay and continue to grow steadily throughout the experiment, indicating oxidation of the Li negative electrode even during relaxation.

Despite extensive research, many questions remain regarding lithium dendrite formation and the physicochemical processes that determine plating behavior. A combination of observational methods is required to further analyze lithiation, and in operando synchrotron XRD is demonstrated to provide valuable insight into the crystalline chemistries of dendrite formation.

Acknowledgements

I would like to thank Martijn van Hulzen for his great guidance, positive attitude, wit and support throughout this project. I also thank Niels van Dijk for countless patient explanations of the solid-state and XRD physics. My fellow (PhD)-students for great discussions and a great time. And last but not least great thanks to Marnix Wagemaker for his thoughts and support, and vision with this dynamic and joyous research group that I will never forget.

Literature

[1] M. Mengel, A. Nauels, J. Rogelj, C.-F. Schleussner, Committed sea-level rise under the Paris Agreement and the legacy of delayed mitigation action, Nature Communications 9 (1) (2018) 601. doi:10.1038/s41467-018-02985-8.
URL http://www.nature.com/articles/s41467-018-02985-8

[2] N. Oreskes, The Scientific Consensus on Climate Change: How Do We Know We're Not Wrong?, in: Climate Modelling, Springer International Publishing, Cham, 2018, pp. 31–64. doi:10.1007/978-3-319-65058-6_2.
URL http://link.springer.com/10.1007/978-3-319-65058-6{_}2

[3] M. Wagemaker, F. M. Mulder, Properties and Promises of Nanosized Insertion Materials for Li-Ion Batteries, Accounts of Chemical Research 46 (5) (2013) 1206–1215. doi:10.1021/ar2001793.
URL http://pubs.acs.org/doi/10.1021/ar2001793

[4] B. Dunn, H. Kamath, J.-M. Tarascon, Electrical energy storage for the grid: a battery of choices., Science (New York, N.Y.) 334 (6058) (2011) 928–35. doi:10.1126/science.1212741.
URL http://www.ncbi.nlm.nih.gov/pubmed/22096188

[5] J. B. Goodenough, Energy storage materials: A perspective, Energy Storage Materials 1 (2015) 158–161. doi:10.1016/J.ENSM.2015.07.001.
URL https://www.sciencedirect.com/science/article/pii/S2405829715300404

[6] A. Yoshino, The Birth of the Lithium-Ion Battery, Angewandte Chemie International Edition 51 (24) (2012) 5798–5800. doi:10.1002/anie.201105006.
URL http://doi.wiley.com/10.1002/anie.201105006

[7] J. M. Tarascon, M. Armand, Issues and challenges facing rechargeable lithium batteries., Nature 414 (6861) (2001) 359–67. doi:10.1038/35104644.
URL http://www.ncbi.nlm.nih.gov/pubmed/11713543

[8] M. Armand, J.-M. Tarascon, Building better batteries, Nature 451 (7179) (2008) 652–657. doi:10.1038/451652a.
URL http://www.nature.com/articles/451652a

[9] Y. Zhang, W. Luo, C. Wang, Y. Li, C. Chen, J. Song, J. Dai, E. M. Hitz, S. Xu, C. Yang, Y. Wang, L. Hu, High-capacity, low-tortuosity, and channel-guided lithium metal anode., Proceedings of the National Academy of Sciences of the United States of America 114 (14) (2017) 3584–3589. doi:10.1073/pnas.1618871114.
URL http://www.ncbi.nlm.nih.gov/pubmed/28320936http://www.pubmedcentral.nih.gov/articlerender.fcgi?artid=PMC5389307

[10] X.-B. Cheng, R. Zhang, C.-Z. Zhao, Q. Zhang, Toward Safe Lithium Metal Anode in Rechargeable Batteries: A Review, Chemical Reviews 117 (15) (2017) 10403–10473. doi:10.1021/acs.chemrev.7b00115.
URL http://pubs.acs.org/doi/10.1021/acs.chemrev.7b00115

[11] W. Liu, D. Lin, A. Pei, Y. Cui, Stabilizing Lithium Metal Anodes by Uniform Li-Ion Flux Distribution in Nanochannel Confinement, Journal of the American Chemical Society 138 (47) (2016) 15443–15450. doi:10.1021/jacs.6b08730.
URL http://pubs.acs.org/doi/10.1021/jacs.6b08730

[12] J.-G. Zhang, W. Xu, W. A. Henderson, Lithium Metal Anodes and Rechargeable Lithium Metal Batteries, Vol. 249 of Springer Series in Materials Science, Springer International Publishing, Cham, 2017. doi:10.1007/978-3-319-44054-5.
URL http://link.springer.com/10.1007/978-3-319-44054-5

[13] K. J. Harry, D. T. Hallinan, D. Y. Parkinson, A. A. MacDowell, N. P. Balsara, Detection of subsurface structures underneath dendrites formed on cycled lithium metal electrodes, Nature Materials 13 (1) (2014) 69–73. doi:10.1038/nmat3793.
URL http://www.nature.com/articles/nmat3793

[14] W. Zhou, S. Wang, Y. Li, S. Xin, A. Manthiram, J. B. Goodenough, Plating a Dendrite-Free Lithium Anode with a Polymer/Ceramic/Polymer Sandwich Electrolyte, Journal of the American Chemical Society 138 (30) (2016) 9385–9388. doi:10.1021/jacs.6b05341.
URL http://pubs.acs.org/doi/10.1021/jacs.6b05341

[15] K. Zhang, G.-H. Lee, M. Park, W. Li, Y.-M. Kang, Recent Developments of the Lithium Metal Anode for Rechargeable Non-Aqueous Batteries, Advanced Energy Materials 6 (20) (2016) 1600811. doi:10.1002/aenm.201600811.
URL http://doi.wiley.com/10.1002/aenm.201600811

[16] D. Rehnlund, F. Lindgren, S. Böhme, T. Nordh, Y. Zou, J. Pettersson, U. Bexell, M. Boman, K. Edström, L. Nyholm, Lithium trapping in alloy forming electrodes and current collectors for lithium based batteries, Energy & Environmental Science 10 (6) (2017) 1350–1357. doi:10.1039/C7EE00244K.
URL http://xlink.rsc.org/?DOI=C7EE00244K

[17] Z.-i. Takehara, Future prospects of the lithium metal anode, Journal of Power Sources 68 (1) (1997) 82–86. doi:10.1016/S0378-7753(96)02546-3.
URL https://www.sciencedirect.com/science/article/pii/S0378775396025463

[18] D. Lin, Y. Liu, Y. Cui, Reviving the lithium metal anode for high-energy batteries (2017). doi:10.1038/nnano.2017.16.

[19] C.-P. Yang, Y.-X. Yin, S.-F. Zhang, N.-W. Li, Y.-G. Guo, Accommodating lithium into 3D current collectors with a submicron skeleton towards long-life lithium metal anodes, Nature Communications 6 (1) (2015) 8058. doi:10.1038/ncomms9058.
URL http://www.nature.com/articles/ncomms9058

[20] W. Li, H. Yao, K. Yan, G. Zheng, Z. Liang, Y.-M. Chiang, Y. Cui, The synergetic effect of lithium polysulfide and lithium nitrate to prevent lithium dendrite growth, Nature Communications 6 (1) (2015) 7436. doi:10.1038/ncomms8436.
URL http://www.nature.com/articles/ncomms8436

[21] D. Aurbach, E. Zinigrad, Y. Cohen, H. Teller, A short review of failure mechanisms of lithium metal and lithiated graphite anodes in liquid electrolyte solutions, Solid State Ionics 148 (3-4) (2002) 405–416. doi:10.1016/S0167-2738(02)00080-2.
URL https://www.sciencedirect.com/science/article/pii/S0167273802000802

[22] W. Xu, J. Wang, F. Ding, X. Chen, E. Nasybulin, Y. Zhang, J.-G. Zhang, Lithium metal anodes for rechargeable batteries, Energy Environ. Sci. 7 (2) (2014) 513–537. doi:10.1039/C3EE40795K.
URL http://xlink.rsc.org/?DOI=C3EE40795K

[23] G. Zheng, C. Wang, A. Pei, J. Lopez, F. Shi, Z. Chen, A. D. Sendek, H.-W. Lee, Z. Lu, H. Schneider, M. M. Safont-Sempere, S. Chu, Z. Bao, Y. Cui, High-Performance Lithium Metal Negative Electrode with a Soft and Flowable Polymer Coating, ACS Energy Letters 1 (6) (2016) 1247–1255. doi:10.1021/acsenergylett.6b00456.
URL http://pubs.acs.org/doi/10.1021/acsenergylett.6b00456

[24] Y. Li, Y. Li, A. Pei, K. Yan, Y. Sun, C.-L. Wu, L.-M. Joubert, R. Chin, A. L. Koh, Y. Yu, J. Perrino, B. Butz, S. Chu, Y. Cui, Atomic structure of sensitive battery materials and interfaces revealed by cryo-electron microscopy., Science (New York, N.Y.) 358 (6362) (2017) 506–510. doi:10.1126/science.aam6014.
URL http://www.ncbi.nlm.nih.gov/pubmed/29074771

[25] D. Lin, J. Zhao, J. Sun, H. Yao, Y. Liu, K. Yan, Y. Cui, Three-dimensional stable lithium metal anode with nanoscale lithium islands embedded in ionically conductive solid matrix., Proceedings of the National Academy of Sciences of the United States of America 114 (18) (2017) 4613–4618. doi:10.1073/pnas.1619489114.
URL http://www.ncbi.nlm.nih.gov/pubmed/28416664http://www.pubmedcentral.nih.gov/articlerender.fcgi?artid=PMC5422797

[26] C. Baehtz, T. Buhrmester, N. Bramnik, K. Nikolowski, H. Ehrenberg, Design and performance of an electrochemical in-situ cell for high resolution full-pattern X-ray powder diffraction, Solid State Ionics 176 (17-18) (2005) 1647–1652. doi:10.1016/J.SSI.2005.03.021.
URL https://www.sciencedirect.com/science/article/pii/S0167273805000974

[27] J. Nelson, S. Misra, Y. Yang, A. Jackson, Y. Liu, H. Wang, H. Dai, J. C. Andrews, Y. Cui, M. F. Toney, In Operando X-ray Diffraction and Transmission X-ray Microscopy of Lithium Sulfur Batteries, Journal of the American Chemical Society 134 (14) (2012) 6337–6343. doi:10.1021/ja2121926.
URL http://pubs.acs.org/doi/10.1021/ja2121926

[28] K. N. Wood, E. Kazyak, A. F. Chadwick, K.-H. Chen, J.-G. Zhang, K. Thornton, N. P. Dasgupta, Dendrites and Pits: Untangling the Complex Behavior of Lithium Metal Anodes through Operando Video Microscopy, ACS Central Science 2 (11) (2016) 790–801. doi:10.1021/acscentsci.6b00260.
URL http://pubs.acs.org/doi/10.1021/acscentsci.6b00260

[29] J.-L. Shui, J. S. Okasinski, P. Kenesei, H. A. Dobbs, D. Zhao, J. D. Almer, D.-J. Liu, Reversibility of anodic lithium in rechargeable lithium–oxygen batteries, Nature Communications 4 (2013) 2255. doi:10.1038/ncomms3255.
URL http://www.nature.com/doifinder/10.1038/ncomms3255

[30] J. Steiger, D. Kramer, R. Mönig, Mechanisms of dendritic growth investigated by in situ light microscopy during electrodeposition and dissolution of lithium, Journal of Power Sources 261 (2014) 112–119. doi:10.1016/J.JPOWSOUR.2014.03.029.
URL https://www.sciencedirect.com/science/article/pii/S0378775314003425

[31] S. Lyu, T. Verhallen, F. Ooms, Y. Xu, Z. Li, Z. Li, M. Wagemaker, Monitoring the lithium spatial distribution in li-metal anodes, Submitted to Nature Communications, awaiting review.

[32] Y.-S. Hong, N. Li, H. Chen, P. Wang, W.-L. Song, D. Fang, In operando observation of chemical and mechanical stability of Li and Na dendrites under quasi-zero electrochemical field, Energy Storage Materials 11 (2018) 118–126. doi:10.1016/J.ENSM.2017.10.007.
URL https://www.sciencedirect.com/science/article/pii/S2405829717303756

[33] W. H. Zachariasen, Theory of X-ray diffraction in crystals, Dover Publications,, New York :, 1945.

[34] B. B. He, Two-dimensional x-ray diffraction, Wiley, Hoboken, USA.

[35] R. Jenkins, R. L. R. L. Snyder, Introduction to X-ray powder diffractometry, John Wiley & Sons, Inc, New York :, 1996.

[36] B. E. Warren, X-ray diffraction, Dover Publications, New York, USA, 1990.

[37] D. S. Sivia, Elementary scattering theory : for X-ray and neutron users, Oxford University Press, Oxford :, 2011.

[38] J. Als-Nielsen, D. McMorrow, Elements of Modern X-ray Physics, John Wiley & Sons, Inc., Hoboken, NJ, USA, 2011. doi:10.1002/9781119998365.
URL http://doi.wiley.com/10.1002/9781119998365

[39] B. Fultz, J. Howe, Transmission Electron Microscopy and Diffractometry of Materials, Graduate Texts in Physics, Springer Berlin Heidelberg, Berlin, Heidelberg, 2013. doi:10.1007/978-3-642-29761-8.
URL http://link.springer.com/10.1007/978-3-642-29761-8

[40] B. D. Cullity, S. R. Stock, Elements of x-ray diffraction, Prentice Hall, Upper Saddle River, NJ :, 2001.

[41] F. H. Chung, D. K. Smith, Industrial applications of X-ray diffraction, Marcel Dekker, New York :, 2000.

[42] S. Ganapathy, J. R. Heringa, M. S. Anastasaki, B. D. Adams, M. van Hulzen, S. Basak, Z. Li, J. P. Wright, L. F. Nazar, N. H. van Dijk, M. Wagemaker, Operando Nanobeam Diffraction to Follow the Decomposition of Individual Li2O2 Grains in a Nonaqueous Li–O2 Battery, The Journal of Physical Chemistry Letters 7 (17) (2016) 3388–3394. doi:10.1021/acs.jpclett.6b01368.
URL http://pubs.acs.org/doi/10.1021/acs.jpclett.6b01368

[43] TU Graz, Atomic form factors.
URL https://lampx.tugraz.at/{~}hadley/ss1/crystaldiffraction/atomicformfactors/formfactors.php

Appendix A:
Theory of X-ray diffraction

Crystal structure

A solid with periodically repeating and regular arrangement of atoms, ions or molecules in three dimensions is called a crystal. The smallest entity within a crystal is called a unit cell, which is described by three non-coplanar vectors $\boldsymbol{a_1}$, $\boldsymbol{a_2}$, and $\boldsymbol{a_3}$ connecting one lattice point to the next. In this way, a repeating pattern of unit cells makes up a crystal. Viewing a crystal as an infinite repetition of a three-dimensional array of points is helpful in understanding it as a lattice, and its reciprocal space counterpart later on. The lattice vectors make an inter-axial angle of α between $\boldsymbol{a_2}$ and $\boldsymbol{a_3}$, β with $\boldsymbol{a_1}$ and $\boldsymbol{a_3}$, and γ between $\boldsymbol{a_1}$ and $\boldsymbol{a_2}$. A crystal is a volume element, and characteristics of the faces do not influence the crystal itself. However, crystal planes are important characteristics within the crystal. The law of rational indices allows for the description of these planes as small integers so that when a lattice point is chosen as the origin, any arbitrary atom in the crystal can be described by positive or negative integer multiples $h\boldsymbol{a} + k\boldsymbol{a_2} + l\boldsymbol{a_3}$, where h, k, l are called Miller indices.
The lattice can be conveniently described in reciprocal space by dividing the cross product of two lattice vectors by the volume of the unit cell $\nu = \boldsymbol{a_1} \cdot (\boldsymbol{a_2} \times \boldsymbol{a_3})$ of the three lattice vectors, like so:

$$\boldsymbol{b_1} \equiv 2\pi \frac{\boldsymbol{a_2} \times \boldsymbol{a_3}}{\boldsymbol{a_1}(\boldsymbol{a_2} \times \boldsymbol{a_3})},\ \boldsymbol{b_2} \equiv 2\pi \frac{\boldsymbol{a_3} \times \boldsymbol{a_1}}{\boldsymbol{a_1}(\boldsymbol{a_2} \times \boldsymbol{a_3})},\ \boldsymbol{b_3} \equiv 2\pi \frac{\boldsymbol{a_1} \times \boldsymbol{a_2}}{\boldsymbol{a_1}(\boldsymbol{a_2} \times \boldsymbol{a_3})} \tag{1}$$

meaning that the sets of vectors are mutually reciprocal[33]. This makes $\boldsymbol{a_n}$ perpendicular to $\boldsymbol{b_n}$, and for example for the following relationship to hold:

$$\boldsymbol{a_1} \cdot \boldsymbol{b_1} = \boldsymbol{a_2} \cdot \boldsymbol{b_2} = 2\pi \tag{2}$$

Bragg's Law

When a crystal is placed within a beam, it can be viewed as a three-dimensional diffraction grating. The lattice reflects incoming waves at a certain angle, and when this angle makes the reflected wave of the next reflecting plane to be exactly travel an integer multiple of the wavelength longer, constructive interference occurs. The reciprocal relationship of Fourier transforms means that reflection will occur when the Fourier transform of the momentum transfer cross section $\boldsymbol{Q}$ lies on a lattice point of the reciprocal lattice. $\boldsymbol{Q}$ is a reciprocal space vector with units of inverse distance and is defined as the wavevector after the scattering event $\boldsymbol{k}_f$ minus the initial wavevector $\boldsymbol{k}_i$, where the scattering angle is conventionally and conveniently defined as $2\theta_B$. In the case of elastic scattering, which will be explained below, no momentum is lost so that $|\boldsymbol{k}_i| = |\boldsymbol{k}_f| = 2\pi/\lambda$. It follows from simple geometry then that

$$|\boldsymbol{Q}| = 4\pi \frac{sin\theta_B)}{\lambda} \tag{3}$$

To see this relation in a 3D reciprocal lattice, we take the initial wavevector

$$\boldsymbol{k}_i = \frac{2\pi}{\lambda} \begin{pmatrix} 1 \\ 0 \\ 0 \end{pmatrix} \tag{4}$$

which leads to a deflected wavevector of

$$\boldsymbol{k}_f = \frac{2\pi}{\lambda} \begin{pmatrix} cos2\theta \\ sin2\theta sin\phi \\ sin2\theta cos\phi \end{pmatrix} \tag{5}$$

Since any point on the reciprocal lattice can then be defined as hkl multiples of the reciprocal lattice vectors, and constructive interference will take place if $\boldsymbol{Q}$ is on a reciprocal lattice point, the following relationship must hold:

$$\boldsymbol{Q} = h\boldsymbol{b_1} + k\boldsymbol{b_2} + l\boldsymbol{b_3} \tag{6}$$

The distance between lattice planes is called the d-spacing, and a distance d equals $2\pi/d$ in reciprocal space, and since $\boldsymbol{Q}$ is satisfied when it lies on a crystal plane thus

$$|\boldsymbol{Q}| = \frac{2\pi\, n}{d} \tag{7}$$

where n denotes that when a multiple of $\boldsymbol{Q}$ is on a reciprocal lattice point, constructive interference will also take place. Equalling this with equation 3 leads to what is known as Bragg's law:

$$n\lambda = 2d \sin\theta_B \tag{8}$$

This marks the importance of the d-spacing. Since the Bragg angle θ_B is the angle between the diffracted beam and the reflection plane for which Bragg's law is satisfied, and sinθ can't exceed unity, Bragg's law can only be satisfied when $\lambda < 2d$.
The distance between lattice planes d_{hkl}, can then be described as follows

$$d_{hkl} = \sqrt{\left(\frac{a_1}{h}\right)^2 + \left(\frac{a_2}{k}\right)^2 + \left(\frac{a_3}{l}\right)^2} \tag{9}$$

Electron Scattering

To see how the diffraction condition can be met, and to derive the characteristics of the scattering object from the scattered intensity, we must consider what occurs in a scattering event, and how interference affects incoming and scattered waves. Photons can be seen as waves of electromagnetic radiation that have oscillating and perpendicular electric $\boldsymbol{E}$ and magnetic $\boldsymbol{H}$ fields[34]. The electric field interact with the negative charge of electrons, whereas the magnetic field interacts with other magnetic fields and is of no significance in X-ray diffraction[35]. Electrons bound to an atom have a fixed energy as dictated by the laws of quantum mechanics, and depending on the available states there are available for an electron after the scattering event, an electromagnetic wave may either be absorbed or scattered. When it is scattered, the resultant change in its momentum $\boldsymbol{P}$ and energy E are defining characteristics, as this is exchanged with the particle it scattered on. When no energy is transferred, that is, the photon retains its momentum, is called *coherent*, elastic or Thomson scattering. The case in which a photon loses part of its energy is called incoherent, inelastic or Compton scattering. The total scattering σ comprises both elastic and inelastic scattering, and they are related through[35]:

$$\sigma = Zf^2 + (1 - f^2) \tag{10}$$

In which coherent scattering is the first term and incoherent scattering the second. f is the atomic scattering factor, which will be expanded on below. For X-ray diffraction we are interested only in coherent scatter, as this is what contributes to the observed Bragg reflections.
J.J. Thompson showed in 1906 that an unpolarized wave scattered from an electron has a total intensity

$$I = \frac{I_0}{r^2} r_e^2 \frac{1 + cos^2(2\theta)}{2} \tag{11}$$

Where I_0 is the incident wave and r^2 is the distance between the scattering event and the point of observation. The last term is called the polarization factor P, which is a consequence of the fact that the scattering depends on the orientation of the polarization of the incoming wave. The constant r_e, is

called the classical radius of an electron or also known as the Thomson Scattering Length and defined as

$$r_e = \frac{e^2}{4\pi\epsilon_0 m_e c^2} \approx 2.818 \cdot 10^{-15}[\text{m}] \tag{12}$$

Where e is the charge of an electron, ϵ_0 is the permittivity of vacuum, m_e is the electron mass and c is the speed of light in vacuum. This term is derived from Maxwell's electrodynamic theory and is the only thing that differentiates neutron from electron scattering[35].
Equation (11) assumes scattering under classical theory, but given the fact that Compton scatter contribute only to diffuse scattering, we have to include a factor that accounts for this. For a complete derivation of the scattering factor per electron, see Warren[36], but we will start by considering the scatter from one atom, called the atomic scattering factor

$$f = \int e^{i\boldsymbol{Q}\cdot r}\rho dV \tag{13}$$

The integral $\int \rho dV$ equals the number of electrons Z charge by definition, as it is a volume integration over the charge distribution of 1 electron.
It becomes evident that when all electrons fully contribute to the scattering wave, the atomic scattering factor approaches the atomic number, as there are this many electrons from which scattering can occur. The atomic scattering factor thus is a function of the electron density distribution. Because we are interested in elastic scatter, in which the energy transfer is defined to be zero, time is completely undetermined, as these are conjugate variables. To gain insight in the scattering we therefore take the Fourier transform of the scattering length density distribution of an atom, on the assumption of spherical symmetry, by which we arrive at the following equation for the atomic scattering factor[37], and we see that it is exactly of the form of that of a single electron, but now includes a scattering length density ρ, which contains the electron charge distribution as a function of the distance $\boldsymbol{r}$ from the atom center.

$$f(\mathbf{Q}) = \iiint \rho(\mathbf{r}) e^{i\mathbf{Q}\cdot\mathbf{r}} \mathrm{d}^3\mathbf{r} \tag{14}$$

in which the electron charge density is described by Schrodinger's wave function Ψ

$$\rho(\boldsymbol{r}) = \left|\Psi^2\right| \tag{15}$$

To complete the atomic scattering factor, we need to look at the lattice vibrations that give rise to a further decrease in scattered intensity.

Lattice vibrations

In an ideal diffraction setup, one would observe distinct diffraction spots where constructive interference takes place and nothing at other locations because of the destructive interference at non-Bragg angles. However, because in reality crystals are of finite size, and an increasing temperature causes increasingly non-trivial lattice vibrations that displace the atoms, there is also diffuse scattering in between reflection spots. This so-called background by thermal diffuse scattering (TDS) is a function of the ratio between the displacement of the atom and the d-spacing of the reflection. Therefore at higher hkl reflections, the thermal scattering has an increasingly strong effect on the reflected intensity. The Debye-Waller factor accounts for these displacements, and is based on the amplitude of the vibrations. Vibrations of the atoms in a crystal are described as displacements from their average position u. The value of u differs per atom and per bond, but generally lighter atoms tend to have larger displacements, and displacements are larger perpendicular to bonds than in the plane of the bond, since changing a bond angle costs less energy than changing a bond length. The vibrations are present even at zero degrees Kelvin, and at

this temperature are called zero-point fluctuations. They increase as the temperature increases, and this leads us to a correction of the atomic form factor at zero Kelvin as follows [36,38]:

$$f = f_0 e^{-\frac{1}{2}\boldsymbol{Q}^2\left\langle u_Q^2\right\rangle} \tag{16}$$

In general $\langle u\rangle$ is the mean displacement, equalling zero by definition. The component of the displacement u parallel to $\boldsymbol{Q}$ is $\langle u_Q\rangle$ and $\left\langle u_Q^2\right\rangle$ is the mean-square amplitude of that displacement. The term in the exponent $\frac{1}{2}\boldsymbol{Q}^2\left\langle u_Q^2\right\rangle$ is called the Debye-Waller factor, and is often denoted as M. We will assume the vibrations to be isotropic, so that $\left\langle u^2\right\rangle = \left\langle u_x^2 + u_y^2 + u_z^2\right\rangle = 3\left\langle u_x^2\right\rangle = \left\langle u_Q^2\right\rangle$, leading to the Debye-Waller factor for an atom of

$$M = \frac{1}{6}\boldsymbol{Q}^2\left\langle u^2\right\rangle \tag{17}$$

The value of u can be experimentally determined, calculated from quantum physics simulations, or approximated using the documented Debye temperature Θ_D of a solid. It is important to note that zero-point fluctuations start to play a significant role when the temperature of the solid is less than approximately $\Theta_D/2$ [39].

Structure Factor

The summation of the atomic scattering factors over the number of atoms in a crystal N, multiplied by their position in the crystal with respect to a reflection plane, gives the structure factor F_{hkl} of that crystal, of which the amplitude squared relates to the reflected intensity of a specific hkl. In other words, F_{hkl} describes the structure of the reciprocal lattice in relationship to the wavevector transfer $\mathbf{Q}$.

$$F_{hkl} = \sum_{j=1}^{N} f_j \mathrm{e}^{-2\pi i(hx_j+ky_j+lz_j)} e^{-M_j} \tag{18}$$

It is a scattered wave, and its amplitude is a function of the electron density in planes parallel to Bragg planes, while its phase describes to what extent these are aligned [35].
Depending on the electron density distribution, interactions between scattering events from different atoms in a crystal can exactly lead to destructive interference in certain cases when the Bragg condition is met. The product of the structure factor with its complex conjugate leads to real expectation values for scattered intensity of a Bragg reflection, and therefore

$$I \propto |F_{hkl}|^2 \tag{19}$$

It is then evident that certain hkl reflections will have a zero-valued phase-term, leading to a scattered intensity of zero.

Lorentz-Polarization factor

We have seen that the polarization of the beam leads to a decreased intensity of a peak with increasing $2\theta_B$ angle in equation 11. There however are other effects of the incident angle on the reflected intensity. To account for the fact that the time a crystal will satisfy the Bragg condition is dependent on the orientation of the crystal with respect to the incoming beam, the Lorentz factor can be derived. The intensity of a reflection from a specific hkl would according to the Bragg's law be a delta peak, however, in reality it has a finite width. Assuming the beam to cover the entire crystal that is in diffracting position, the anglular range under which appreciable diffraction takes place can be related to the number of repetitions of the lattice constant relevant for the corresponding diffraction plane and the sine of the reflection [40].

$$\Delta\theta = \frac{\lambda}{2N|\boldsymbol{a}|sin\theta_B} \tag{20}$$

The larger this angle $\Delta\theta$, the more the peak will be broadened. Thus the peak intensity I_{max} is proportional to $1/sin\theta$. The fact that crystals are of finite

size causes a broadening that becomes increasingly apparent with smaller crystal size, as the angular range over which incomplete destructive interference of non-bragg angles occurs increases accordingly. Based on this the number of reflection planes and thus the thickness t can be approximated as follows[40]:

$$N\, d_{hkl} \equiv t \approx \frac{0.94\lambda}{Bcos\theta_B} \tag{21}$$

Where the breadth of the reflection at half I_{max} - called full width half maximum (FWHM) is denoted B. Every diffractometer records a finite breadth, even when probing an *ideal* crystal. The value of B for an *ideal* crystal depends on the diffraction angle and on the characteristics of the diffractometer, and X-ray facilities are continuously trying to optimize this instrumental function[41]. The integrated intensity is proportional to the product of I_{max} and B and therefore is related to $1/sin\theta_B$ and $1/\cos\theta_B$ respectively. The rotation of the sample around the vertical axis leads to another correction factor that corresponds to $1/sin\eta$ with η being the angle that the crystal is rotated along the incoming beam. This leads to a Lorentz-Polarization factor for individual crystals of

$$L_g = \frac{1}{sin2\theta_B sin\eta}\frac{1+cos^2(2\theta)}{2} \tag{22}$$

Volume calculations

The integrated intensity of a reflection can be used to determine the volume of the crystal that caused the reflection[36,38,42]. This boils down to the same relationship as equation 11 for single-electron scattering shows, and is only refined for the above discussed factors of crystal size, structure and experimental setup.

For the case of an experiment with a sample that is rotated along a vertical axis, and assuming the sample is thin enough and the wavelength far enough away from absorption edges for the absorption to be negligible and the diffraction to be entirely kinematical (no interaction between incident and diffracted beam), this leads to the following relationship between integrated intensity and the volume of the crystal[36,38,42]:

$$I_g = \Phi_0 r_e^2 \frac{\lambda^3 |F_{hkl}|^2 V_g}{\omega\, \nu^2} L_g \tag{23}$$

In the above Φ_0 is the incident flux $[m^{-2}s^{-1}]$, V_g the volume of the grain of which the reflection is observed in [Å^3], ω the angular velocity in $[rad\, s^{-1}]$.

Which is rewritten to obtain the flux, which will be used to determine the volume of an individual grain with the following equation:

$$V_g = \frac{I_g}{\Phi_0}\frac{\omega\, \nu^2}{r_e^2 \lambda^3 |F_{hkl}|^2 L_g} \tag{24}$$

The integrated intensity I_g of a grain was obtained by determining a background for each frame, and setting all pixels that are less than 1.25 times that to zero. In this way the intensity of grains that would fall below - but is set to zero approximately equals that of the outliers in the positive side. This method seems rather arbitrary but was visually confirmed to be more effective than using an integer multiple of the standard deviation.

Applications

In order to calculate the volume of a single grain, the flux was determined using the known quantity of copper. The Cu111 reflection was used because it is the brightest and thus the least susceptible to noise. The intensity of a powder ring reflection is given by[42]:

$$I_p = \Phi_0 r_e^2 \lambda^3 \frac{m_{hkl}|F_{hkl}|^2 V_{gauge}}{\nu^2} L_p \tag{25}$$

The unit cell of copper contains 4 atoms, in an FCC lattice. The structure factor therefore is $4f_{cu}$ for a visible reflection, where f_{cu} was determined using the Gaussian approximations of Vol C of the International Tables for Crystallography, available online at[43], combined with the vibrations u as computed using density functional theory (DFT).

The probed volume is the amount of crystalline copper that is exposed to the incident beam. This is a function of the thickness of the copper plate, the porosity and the cross-sectional area of the beam. In this case, it concerns twice a copper film of 18 μm, a porosity of 3%, and a beam area of 5 μm^2, leading to a gauged volume of ~ 170 cubic microns, or $1.7{\cdot}10^{14}$ Å^3. This was then validated by calculating the flux on 55 LiFePO4 reflections with a known average diameter of 1400 Å. The flux that was obtained with this method is $\sim 2.0(5){\cdot}10^{22}\, [m^{-2}\, s^{-1}]$.